

# Journal Name

## ARTICLE TYPE

Cite this: DOI: 00.0000/xxxxxxxxxx

### Leveraging high-resolution spatial features in mid-infrared spectroscopic imaging to classify tissue subtypes in ovarian cancer<sup>†</sup>

.....\*

Received Date  
Accepted Date

DOI: 00.0000/xxxxxxxxxx

Chalapathi Charan Gajela,<sup>a</sup> Matthew Brun,<sup>b</sup> Rupali Mankar,<sup>a</sup> Noah Kennedy,<sup>c</sup> Sara Corvigno,<sup>d</sup> Yanping Zhong,<sup>d</sup> Jinsong Liu,<sup>d</sup> Anil K. Sood,<sup>d</sup> David Mayerich,<sup>a</sup> Sebastian Berisha,<sup>c</sup> and Rohith Reddy<sup>\*a</sup>

Mid-infrared spectroscopic imaging (MIRSI) is an emerging class of label-free techniques being leveraged for digital histopathology. Optical photothermal infrared (O-PTIR) is based on vibrational absorbance imaging using a pump-probe architecture capable of a 10 $\times$  enhancement in spatial resolution relative to FTIR imaging. This allows truly sub-cellular spectroscopic investigation of tissue at biochemically important fingerprint wavelengths. Modern histopathologic identification of ovarian cancer involves tissue staining followed by morphological pattern recognition. This process is time-consuming, subjective, and requires extensive expertise. In this paper, we present the first label-free automated histological classification of ovarian tissue sub-types using MIRSI. We demonstrate that enhanced resolution of sub-cellular features, combined with spectroscopic information, enables reliable classification (0.98 AUC) of ovarian cell sub-types. Moreover, we present statistically robust validation from 74 patient samples with over 60 million data points. This demonstrates that sub-cellular resolution from five wavenumbers is sufficient to outperform state-of-the-art diffraction-limited techniques from up to 374 different wavenumbers. O-PTIR also performs measurements in back-reflection geometry, opening the door to future *in vivo* studies on glass slides.

## 1 Introduction

Epithelial ovarian cancer is the leading cause of death among gynecological malignancies in the United States. Serous ovarian cancer, its most common subtype, is often diagnosed at late stage (III or IV) where 5-year survival is 51% and 29% respectively.<sup>1</sup> Standard treatments involve surgery and at least six courses of chemotherapy containing platinum.<sup>2</sup> Several novel compounds have been studied and approved over the past 20 years, however none substantially modify overall survival.<sup>3</sup> The strongest prognostic factor remains complete eradication of neoplastic tissue through radical surgery.<sup>4-6</sup> This is affected by (1) late diagnosis resulting in unresectable disease, and (2) unclear identification of neoplastic margins. Objective and early identification of neo-

plastic tissue is therefore essential for optimal surgical attempts.

Recent advances reveal the complex organization of the ovarian tumor microenvironment, highlighting inter-cellular pathways<sup>7</sup> as potential treatment targets. New methods quantifying biomolecular characteristics reveal detailed structural and molecular changes that may reveal novel therapeutic targets. The current standard for ovarian cancer diagnosis uses contrast-inducing stains on biopsy sections followed by microscopic examination by a pathologist. Hematoxylin and eosin (H&E) is widely used to identify cellular and extracellular components. *Epithelial* carcinoma is the most common histologic type, accounting for about 90 percent of cancers of the ovary, fallopian tube, and peritoneum.<sup>8,9</sup> In high-grade serous carcinoma (HGSC), a pathologist identifies a variety of architectural patterns including complex papillary, glandular, microcystic, and solid patterns. HGSC infiltrates, destroys, and/or replaces the normal *stroma*. Therefore, histological identification of cellular sub-types is an important step<sup>10</sup> in ovarian cancer diagnosis and prognosis.

Inter-pathologist variability is an important challenge<sup>11</sup> and grading schemes have been proposed to reduce this variability.<sup>12-14</sup> However, these methods have only been successful in resource-rich hospitals with comprehensive training.<sup>15</sup> Au-

<sup>a</sup> Address, 4226 Martin Luther King Boulevard, N308 Engineering Building 1, Houston TX, 77584, USA; E-mail: rkreddy@uh.edu

<sup>b</sup> Address, Address, Town, Country.

<sup>†</sup> Electronic Supplementary Information (ESI) available: [details of any supplementary information available should be included here]. See DOI: 00.0000/00000000.

<sup>‡</sup> Additional footnotes to the title and authors can be included e.g. 'Present address:' or 'These authors contributed equally to this work' as above using the symbols:  $\ddagger$ ,  $\S$ , and  $\P$ . Please place the appropriate symbol next to the author's name and include a \footnotetext entry in the the correct place in the list.

tomated and semi-automated techniques to aid reduce inter-pathologist variability, especially in lower-resource settings, is critical for equitable care.<sup>16-18</sup>

Automated tissue classification into epithelium and stroma sub-types is challenging, and several techniques have been proposed. Most use H&E<sup>19-21</sup> and immunohistochemical staining<sup>22</sup> combined with machine learning (ML). Staining quality and variability can confound ML and lead to inconsistent results.<sup>17</sup> Our goal is to perform label-free recognition of tissue sub-types without the use of chemical contrast agents. Moreover, we obtain intrinsic quantitative and repeatable biochemical measurements that are independent of operator tissue processing.

Spectroscopic techniques are used widely in chemical and biochemical analysis<sup>23</sup> to identify molecules with excellent sensitivity and specificity. Vibrational spectroscopy is used routinely in the identification of organic biomolecules and commercial spectral libraries that identify<sup>24</sup> over 260,000 spectra are now available.

Prior work on ovarian tissue analysis using label-free technologies has utilized spectroscopy without obtaining hyperspectral tissue images. For example, Raman spectroscopy<sup>25-27</sup>, conventional Fourier Transform Infrared (FTIR) spectroscopy<sup>28-30</sup> and attenuated total reflection (ATR) FTIR spectroscopy<sup>31,32</sup> have been used for the detection and diagnosis of ovarian cancer. MALDI imaging<sup>33</sup> has also been used to analyze ovarian histotypes but is tissue destructive. Second-harmonic generation (SHG) has been used to identify collagen in stroma<sup>34-36</sup> and multi-photon microscopy<sup>37</sup> is used on murine tissue. Raman imaging has been used for ovarian cancer diagnosis and tissue analysis, often with added nanoparticles<sup>38,39</sup> to obtain reliable signals. However, these techniques cannot provide classified images of ovarian tissue sub-types in an automated, label-free, quantitative, and non-destructive manner.

Mid-infrared spectroscopic imaging (MIRSI) can extract spectral and spatial information from tissue samples, without the need for staining or external contrast agents. It utilizes intrinsic biochemical information for identification and classification of tissue. Furthermore, the technology is non-destructive and the tissue can be used for independent analysis using complimentary technologies.<sup>40</sup> Fourier transform infrared (FTIR) spectroscopic imaging, the best known MIRSI technology has been used successfully to classify cell subtypes in a variety of diseases including breast,<sup>41</sup> lung<sup>42</sup>, prostate<sup>43</sup>, and colon<sup>44</sup> cancers. We hypothesize that it is also useful to automatically segment and classify ovarian cancer tissue. HGSC is the marked cytologic atypia with prominent mitotic activity in ovarian tissue. The atypical nuclei are hyperchromatic with a threefold or greater variation in nuclear size, and tumor giant cells are common. The phosphate spectroscopic peaks (1080, 1201, 1236, 1262 cm<sup>-1</sup>) corresponding to nucleic acids have a strong correlation to mitotic activity and spectroscopic imaging has been shown to recognize increases mitotic activity in a variety of cancers.<sup>45-47</sup>

FTIR imaging provides a spatial resolution limited by the diffraction-limit of mid-infrared light (2.5 μm - 11 μm). Since typical cells are of 5 μm in size, FTIR imaging cannot provide sub-cellular information that is potentially important to tissue analy-

sis. Recent MIRSI advances have resulted in the development of optical-Photothermal infrared (O-PTIR) imaging that overcome this resolution limitation. This technique combines a visible laser beam and a mid-infrared beam, in a pump-probe architecture and estimates the sample's absorbance by measuring the change in intensity of the visible laser caused by the photothermal effect. Therefore the image resolution is determined by the wavelength of visible light (0.5 μm), which is much shorter than the wavelength of IR light incident on the sample, allowing 5x to 22x improvement in spatial resolution<sup>48</sup>. The improved spatial resolution is comparable to the optical microscope image as demonstrated in Figure 1. This technology has been used previously for studying the chemistry of inorganic 2D perovskite, and allowed us to understand the edge emission phenomenon in inorganic 2D perovskite.<sup>49</sup> O-PTIR has also been successfully used in ultrafast chemical imaging of live human ovarian cancer cells<sup>50</sup>, where high resolution is needed to analyze sub-cellular structures in a small sample. However, our work is the first large scale (74 cancer patient) study of clinical ovarian tissue biopsy samples each with a large sample areas (1 mm diameter each).

Conventional machine learning algorithms, including random forest classifiers (RF) and Bayesian classifiers, use per-pixel spectral data to classify tissue regions. These approaches do not involve the use of spatial information contained in the images. However, MIRSI provides spatial and spectroscopic information simultaneously and requires innovations in classification algorithms for optimal tissue segmentation. Convolutional neural networks (CNNs) are deep learning models that take advantage of the local spatial organization inside the images' to compute their analysis. CNNs have previously demonstrated to be successful in analysing hyperspectral imaging<sup>51</sup> and in mid-infrared spectroscopic tissue classification of breast cancer tissues<sup>52</sup>. Traditional network structures consist of alternating convolution and pooling layers, followed by fully connected layers. In this work, we use CNNs to determine what effect the improved resolution of O-PTIR imaging has on tissue classification algorithms. We report the first application of the O-PTIR technology to tissue classification. Furthermore, IR spectroscopic imaging and CNNs have not previously been applied to tissue histology in ovarian cancer. Previous work in spectroscopic analysis of ovarian cancer has relied on point spectral data for identification of malignant tissue or categorization of cancer grading<sup>27,31</sup>. To the best of our knowledge, this is also the first application of MIRSI to automated histopathologic classification of ovarian cancer tissue.

## 2 Materials and methods

A tissue microarray (TMA) consisting of ovarian tissue biopsies from different patients, obtained from Biomax US, Rockville, MD (TMA ID: BC11115c), and was imaged using O-PTIR spectroscopy. The dataset contained 100 cores from separate patients with cases of normal, hyperplastic, dysplastic, and malignant tumors tissues. The patient cohort was composed of women aged 29 to 69 years; ovarian tumor stages varied between stage I to stage IIIC; histological subtypes included clear cell carcinoma, high-grade serous carcinoma, and Mucinous adenocarcinoma. The paraffin-embedded samples were deparaffinized be-

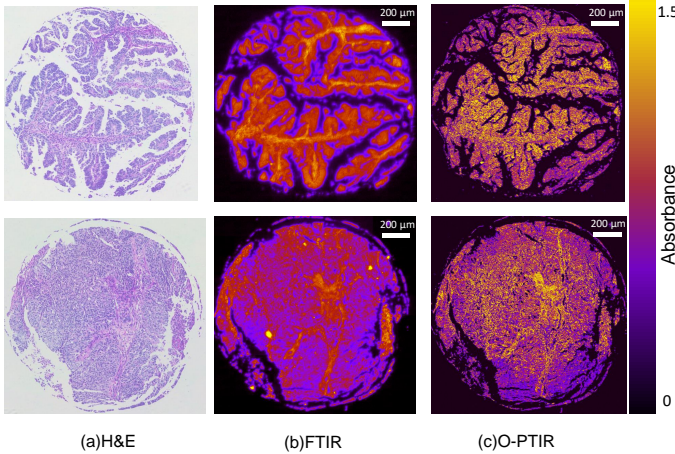


**Fig. 1** Two tissue cores from ovarian cancer patients is stained with H&E and presented in (a). Corresponding tissue images at  $1664\text{ cm}^{-1}$  from FT-IR is presented in (b) and data from O-PTIR is in (c). The figure demonstrates a good correspondence between H&E and spectroscopic imaging data. Moreover, the O-PTIR image has a significantly higher resolution and finer tissue details are visible in (c) relative to images in (b).

fore undergoing O-PTIR imaging. The data was collected using both FTIR and O-PTIR techniques from the eighty deparaffinized tissue biopsies. The corresponding adjacent histological section, stained with H&E, was examined by pathologist expert in the field of ovarian cancer. Cell types were identified from different disease stages. We trained a random forest classifier, Support Vector Machine (SVM), K-Nearest Neighbor (KNN) and a CNN model on each randomly selected pixels from left half of TMA and compared the accuracies of the models by testing it on left half of the TMA.

### 2.1 O-PTIR imaging

Photothermal microscopy obtains a measurement of sample absorbance by estimating the thermal expansion caused by absorption of infrared light using a co-localized visible laser beam. The visible and IR laser are incident on the sample collinearly as shown in Figure 2. The thermal expansion caused in the sample due to IR absorbance causes variation in the refractive index due to the photothermal effect. This change in refractive index is detected by measuring the change in intensity of the back-reflected green laser (visible laser) using a point detector. For the current experiment the optimal settings of 80 percent of maximum IR laser power and 40 percent of maximum green laser power with detector gain of 10x were used to get best signal to noise ratio (SNR) without burning the sample.

### 2.2 Improved Spatial Resolution

FTIR has been the standard spectroscopic imaging technique for characterizing the material's chemistry, while the H&E staining is the clinical gold standard in disease diagnosis. Both of these

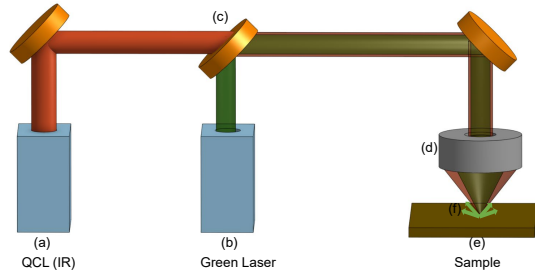


**Fig. 2** Schematic of the optical path of IR and green laser (532 nm) in our O-PTIR instrument. A pulsed Quantum Cascade Laser (QCL) shown in (a) is the source of mid-IR light which acts as a pump causing photothermal expansion at sample. A Continuous Wave (CW) green laser shown in (b) is incident collinearly on the sample and acts as a probe beam. A dichroic mirror (c) combines the green and QCL light and focuses them on the sample (e) using a reflective Cassagrain objective (d). The modulation in intensity of the green light (f) that is scattered back from the sample enables measurement of IR absorbance of the sample.

techniques have their deficiencies, with H&E staining being more qualitative and subjected to possible ambiguity in interpretation. While FTIR provides information from the full range of near and mid-infrared wavenumbers, it is bound by low spatial resolution caused by the diffraction limit. The new O-PTIR technique gets a much higher spatial resolution image comparable to that of the H&E stained image. Figure 3 demonstrates the increase in spatial resolution of O-PTIR image as compared to the FTIR image of the same cancer core and comparable to that of the stained image of the adjacent section of the corresponding cancer core. The spatial differences in different classes of cells are evident in O-PTIR image as shown in Figure 3.

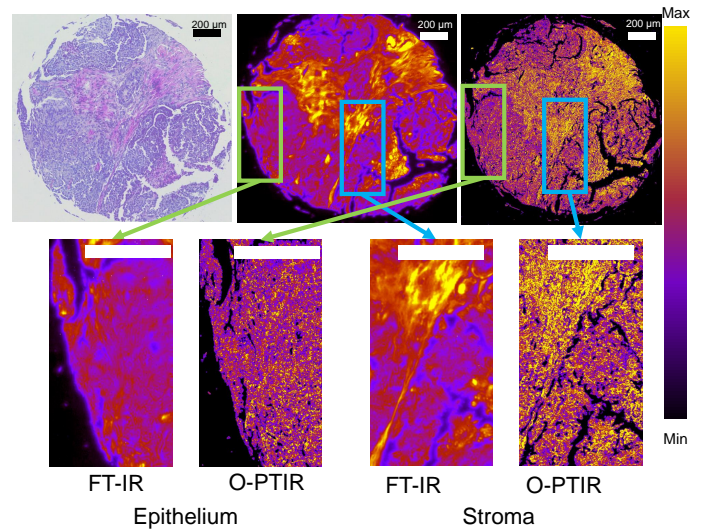


**Fig. 3** Spatial differences between different cell types in FT-IR image on the left, H & E image in the center and O-PTIR image on the right. Cropped regions around pixels from the same core in FT-IR and O-PTIR images collected at  $1650\text{ cm}^{-1}$ .

### 2.3 Data acquisition

FTIR chemical images for the HD dataset of the TMA were acquired using an Agilent Stingray imaging system consisting of a 680-IR spectrometer connected to a 620-IR imaging microscope with a numerical aperture of 0.62. We performed the imaging of each core in the TMA at 16 co-additions in transmission mode. The spectral resolution was  $8\text{ cm}^{-1}$  with a pixel size of  $1.1\text{ }\mu\text{m}$  and a truncated spectral range of  $902\text{ cm}^{-1}$  to  $3892\text{ cm}^{-1}$ . We collected the background scan at 128 co-additions and ratioed to the single beam data to remove spectral contributions from the substrate, atmosphere, and globar source.

The O-PTIR dataset was acquired with a Photothermal mi-Rage microscope with a silicon photodiode, a pixel size of  $0.5\text{ }\mu\text{m}\times 0.5\text{ }\mu\text{m}$  and a 0.65 numerical aperture. A Quantum Cascade Laser (QCL) is the source of IR which sweeps through the range of  $902\text{ cm}^{-1}$  to  $1898\text{ cm}^{-1}$  emitting discrete wavenumbers. Each core was imaged at five selected discrete wavenumbers. The system's focus position does not change during imaging, and the O-PTIR system is highly sensitive to focus position; hence, any tilt in the sample can cause a gradient in data collected. To avoid such issues, we calculated each core's mean focus by taking the mean of the focal position at 4 corners of the core and the center. We used 40% probe laser power and 80% infrared laser power as optimal settings in order to get the highest signal to noise ratio (SNR) without damaging the tissue. An image of the entire TMA acquired at the Amide I band is shown in Figure 4.

We used an Aperio Scanscope system to acquire the Light microscope images of the whole slide's H&E chemically stained sections.

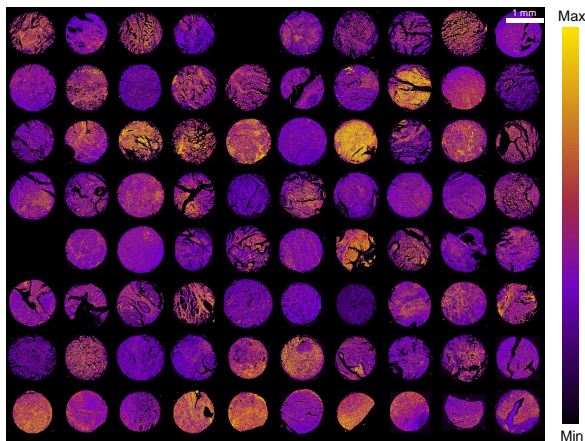


**Fig. 4** O-PTIR microarray ( $8\times 8$ ) shown at band  $1664\text{ cm}^{-1}$ . Data from 70 ovarian cancer patients is shown. The biochemical variations in tissue is evident from differences in color in the figure. Spectral bands provide biochemical information, which, in combination with machine learning enable tissue-subtype identification and disease diagnosis.

### 2.4 Feature Selection

Since the O-PTIR signal is detected using a point detector, the time taken to collect an image of a single core varies between 90 to 100 minutes per wavenumber. Hence collecting the full image of core at all wavenumbers in  $900\text{ cm}^{-1}$  to  $1900\text{ cm}^{-1}$  at  $2\text{ cm}^{-1}$  spacing will take approximately 32 to 35 days. To reduce the time of imaging, we need to collect fewer band images with important biochemical information. These wavenumbers are determined by analyzing FTIR spectra of ovarian tissue to determine absorbance peaks corresponding to major functional groups. Based on this analysis we decided to acquire O-PTIR data at wavenumbers  $1162\text{ cm}^{-1}$ ,  $1234\text{ cm}^{-1}$ ,  $1396\text{ cm}^{-1}$ ,  $1540\text{ cm}^{-1}$ , and  $1661\text{ cm}^{-1}$  (Figure 5), which correspond biochemically to glycogen, amide III, nucleic acids and lipids, amide II, and amide I, respectively<sup>45,53</sup>.

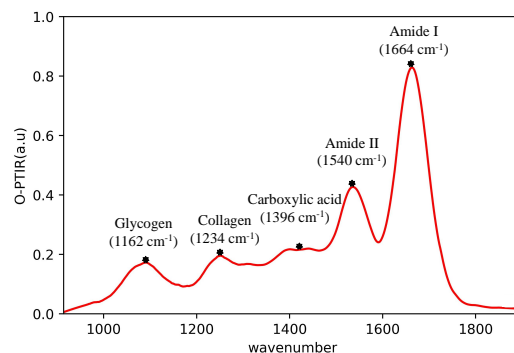


**Fig. 5** The figure shows absorption spectrum of ovarian tissue collected using O-PTIR technique. The spectrum shows the IR absorption values (Y-axis) for the wavenumbers (X-axis) in the fingerprint region. The marked peaks on the spectrum correspond to biochemically relevant functional groups of glycogen at  $1162\text{ cm}^{-1}$ , amide III at  $1234\text{ cm}^{-1}$ , nucleic acids and lipids at  $1396\text{ cm}^{-1}$ , amide II at  $1540\text{ cm}^{-1}$ , and amide I at  $1661\text{ cm}^{-1}$ <sup>53</sup>.

### 2.5 Data pre-processing

The standard preprocessing steps used in FTIR are not used in O-PTIR because the data collected in FTIR is a direct measurement of IR absorption by the sample ratioed to the incident source power while raw data obtained from O-PTIR is an indirect measure of absorption of the IR wavenumber by the sample using a visible laser. Since the power emitted by QCL is not uniform over all the wavenumbers, the background spectra is collected with 10 co-additions to measure the power of different wavenumbers in QCL. The raw data is then normalized with the power spectra value corresponding to its wavenumber from the background spectra. The range of values of raw O-PTIR signal typically vary between 0mV to  $1.5\text{ mV}$  for the current set of parameters mentioned. But there are always few outlier pixels which give very high signal which could be happening due to high reflectivity of green laser from those pixels. This leads to different range of O-PTIR signal values in different cores of TMA. Normalizing all the bands with Amide I band ( $1664\text{ cm}^{-1}$ ) will bring the range between 0 and 1 for all the cores significantly reducing the variation in range caused by those few outlying pixels.

Note that some tissue biopsies are missing because of the collected data was bad and larger areas of epithelium and stroma were intermixed so much that presence of subtypes of stroma or other cells being present in annotations is causing errors.

## 2.6 Data annotation

The tissue cores were labeled by two pathologists on adjacent tissue slices stained with H&E as stroma or epithelium. The provided H&E annotations were used to annotate O-PTIR data by manually aligning the chemically stained annotated image with IR images. To generate training and testing data sets, the left half of TMA was used for training and the right half of the TMA was used for testing to maximize the variety of tissue the classifiers were exposed to while maintaining independent training and testing sets.

## 2.7 Classification Models

As a baseline comparison, an SVM classifier is trained on 10000 randomly selected pixels from training dataset summarized in Table 1. 10,000 samples per class are used to train the classifier to balance the number of samples for each class. Similarly, we trained a random forest classifier with 100 trees using 10,000 samples per class. The inputs to the classifiers were five element vectors containing the IR absorption values at each pixel and the corresponding pixel label. Further increasing the number of samples per class did not show any significant increases in the overall accuracy of these classifiers.

We designed a CNN model based on structure and hyperparameters which have demonstrated success in breast cancer histology<sup>52</sup>. As inputs to the networks, we cropped a  $32 \times 32$  region around the center pixel in O-PTIR data to leverage the local spatial information. The base network structure used consists of a convolution layer with 32-feature maps, followed by a  $2 \times 2$  max-pooling layer, followed by a convolution layer with 32-feature maps and another convolution layer with 64-feature maps, then ends with a fully connected layer with 64 nodes and a softmax layer to output classification probabilities. The network for O-PTIR data contains an extra 32-feature convolution layer and  $2 \times 2$  max pooling layer before the 64-feature convolution layers to adjust to the larger input size, ensuring that the feature size in the final layers are equivalent in both models (Figure 6).

## 2.8 Hyperparameters

We chose the following hyperparameters for the Random Forest model: The random forest classifier is trained on 10000 randomly selected pixels from training dataset summarized in Table 1 with 100 trees. The inputs to the classifiers were five element vectors containing the IR absorption values at each pixel and the corresponding pixel label.

We chose the following hyperparameters for the CNN model:

- Optimization:** The Adam optimizer was used<sup>54</sup>.
- Dropout:** The networks had a dropout layer before the fully connected layer with a keep probability of 0.5. This layer

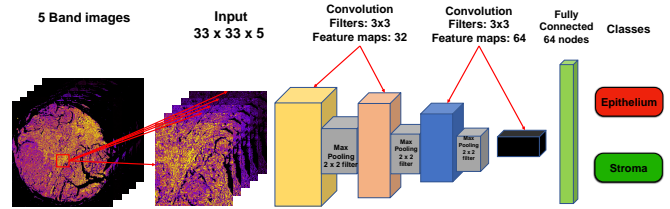


**Fig. 6** Schematic presentation of the CNN architecture used for classification of O-PTIR data. A spatial region of size  $33 \times 33$  is cropped around each pixel. Data cubes of size  $33 \times 33 \times 5$  are fed into the first convolution layer. Each input is convolved with filters of size  $3 \times 3$  outputting 32 feature maps. The following layer is a max pooling layer, which reduces the spatial dimensions by half. Feature extraction continues with three more convolution layers consisting of one 32 and two 64 feature maps consecutively. The extracted features are then flattened and fed to a fully connected layer with 128 units. The last layer, softmax, consisting of 2 units (number of classes) outputs a vector of class probabilities. At the end, maximum probability is used to map each input pixel to its corresponding class labels.

aids regularization and prevents overfitting by randomly disabling nodes in the first and last layers in training. Dropout layer were included before the softmax layer and before the first 64-feature convolution layer.

- Non-linearity:** Rectified Linear Unit (relu) activation function is used as activation function for each layer.
- Weight initialization:** The initial weights of keras layers are initialized using Randomnormal class from the built-in initializer in the module. This initializer generates tensors with a normal distribution with mean at 0.0 and standard deviation of 0.05.
- Batch Size:** The networks trained with a batch size of 128 images.
- Epochs:** The networks were trained for 8 epochs. Data were randomly shuffled between epochs.

## 2.9 Implementation

All data pre-processing was performed using our open-source SProc software<sup>55</sup>, implemented in C++ and CUDA. Training and testing was performed in Python using open-source software packages. The CNNs were implemented in python with the Keras library<sup>56</sup>, built on TensorFlow<sup>57</sup>. Random forest classifiers and accuracy scores were computed using the Scikit-learn library<sup>58</sup>. The experiments were run on a NVIDIA Tesla K40m GPU.

## 3 Results

Considering our primary goal to leverage improved spatial resolution in O-PTIR imaging to classify cell types in O-PTIR images, we used overall accuracy (OA) and receiver operating characteristic (ROC) curves as evaluation metrics. The overall accuracy (OA) would be useful for both binary, and multi-class classification as it represents the percentage of pixels that were mapped correctly to the appropriate class. The ROC curves delineate the correlation between specificity and sensitivity to ascertain acceptable false

positive and true positive indicators. We tested classification algorithms such as RF and SVM, which are spectral-based, and CNN classifier which uses spectral and spatial features on the O-PTIR data. The overall accuracy of these classifiers is compared in Table 2 to evaluate the highest performing classifier. CNN outperforms RF and SVM classifiers in terms of overall and classwise accuracy.

The per class accuracy values and the overall accuracy obtained after classification of testing dataset is summarized in Table 2. The ROC curves and AUC values for all the classifiers and datasets used is shown in Figure 8 where it can be seen that CNN overcomes SVM and RF in AUC values for all the datasets. The overall accuracy with CNN shows a very high improvement of approximately 40-50% in comparison with RF and SVM. The low overall accuracy scores for RF (53.21%) and SVM (45.57%) can be attributed to using spectral information from only 5 wavenumbers instead of all the wavenumbers in the spectrum from 900-1900. Meanwhile the high overall accuracy achieved by CNN (94.61%) is due to utilization of both spectral and spatial features.

**Table 1** The table shows the number of pixels available for training and testing from O-PTIR data, separated by class. Testing and training sets were built by splitting the entire TMA in half and assigning one half to each set. To prevent class bias in training, equivalent numbers of pixels were selected from each class, 10,000 per class in random forest classifiers and, in CNNs, 400,000 pixels per class from O-PTIR data.

Class	Training	Testing
Epithelium	22,766,257	19,249,625
Stroma	11,001,575	8,719,719
Total	33,767,832	27,969,344

**Table 2** Accuracy scores of random forest models by data type across 80 experiments, trained with 10,000 randomly selected samples per class and in CNNs, 400,000 pixels per class. The random forest classifier is much less accurate than the CNN, likely because the increased resolution allows an increase in within-class spectral diversity, making classification more difficult without use of spatial features.

Class	SVM	Random Forest	CNN
Epithelium	$80.31 \pm 0.18$	$60.18 \pm 0.29$	$95.33 \pm 1.52$
Stroma	$29.84 \pm 0.26$	$44.27 \pm 0.21$	$93.00 \pm 1.97$
Total	$45.57 \pm 0.3$	$53.21 \pm 0.05$	$94.61 \pm 0.82$

The classification model obtained from CNN was used to classify the entire TMA of ovarian tissue punches and not only the annotated areas. Figure 7 shows the classification results which are consistent with the H&E stained image dataset. The results show that epithelium and stroma are well classified using the CNN classifier and the distinction in these classes is comparable to that of the visible stained images. In order to quantitate the efficiency of different classifiers, we used Area Under the Curve (AUC) and Receiver Operating Characteristic plot (ROC) curves as metrics. The CNN classifier demonstrates high value with AUC of 0.98 and 0.58 for the RF classifier and the visual representation of ROC is demonstrated in Figure 8.

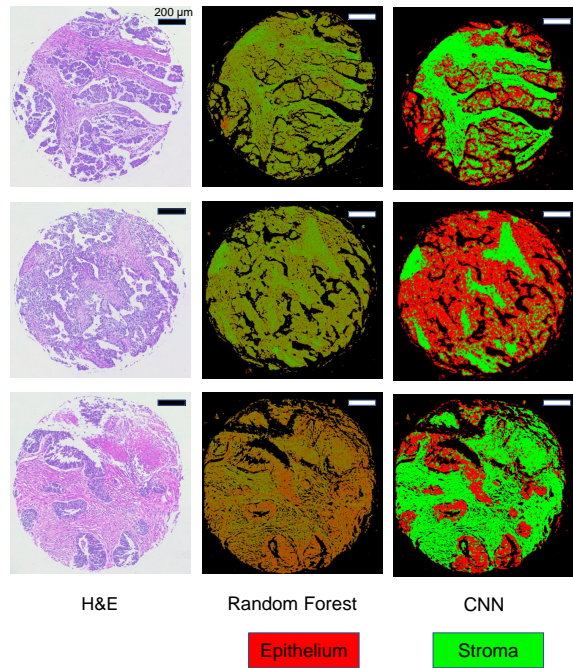


**Fig. 7** O-PTIR classification using a convolutional neural network with both spectral and spatial features. The upper row of the image shows the H&E stained adjacent sections and the lower row shows the Individual classified cores in false-color.

We calculated the ratio of Stroma to Stroma and Epithelium and plotted it against the stage of cancer as shown in Figure 9. Since the stage of cancer is qualitative, we assigned a quantitative variable, and the curve is fitted using non-linear regression to observe the trend in the ratio as a function of the stage of cancer which can be observed from the plot in figure 8 (a). The plot in figure 8 (b) shows the trendline with error bands for each stage, demonstrating the dramatic reduction of stroma during the early stages of cancer relative to normal healthy tissue.

All data pre-processing was performed using our open-source SIproc software<sup>55</sup>, implemented in C++ and CUDA. Training and testing was performed in Python using open-source software packages. The CNNs were implemented in python with the Keras library<sup>56</sup>, built on TensorFlow<sup>57</sup>. Random forest and SVM classifiers and accuracy scores were computed using the Scikit-learn library<sup>58</sup>. The CNN classifier's performance was calculated by testing the classifiers on ten different sets of randomly selected training pixels and averaging the overall accuracy run on a NVIDIA Tesla K40m GPU.

## 4 Discussion

FTIR imaging captures an absorption spectrum across a range of wavenumbers at each point, while O-PTIR allows us to obtain high-resolution absorption images of the sample at discrete wavenumbers. O-PTIR techniques also require more time to scan equivalent areas relative to FTIR, limiting the amount of data that can be reasonably collected. The effect of the improvement in resolution on tissue classification has not yet been studied. The classification accuracy of the CNN model ( $\approx 90\%-94\%$ ) demon-

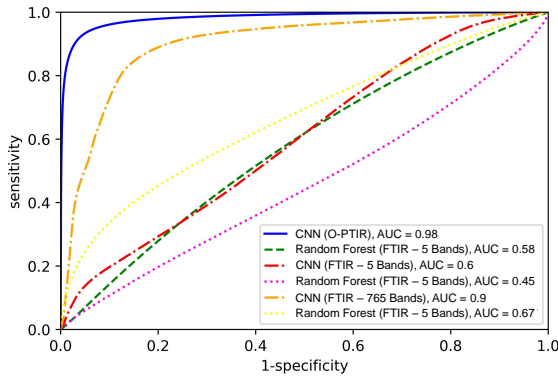


**Fig. 8** ROC curves and associated AUC values for binary classification of tissue type, separated by classifier type and datasets used. Due to the use of two-class models, each tissue class curve is a reflection of the curve from the other class, and thus the AUC values are equal across tissue class. CNN classifiers exhibit superior results to the random forest (RF) classifiers, indicating that spatial information is important in distinguishing tissue types.

strate that ovarian cancer tissue can be classified using spectral and spatial data. While this result has been found in other tissue types, this work extends the technique's application to ovarian tissue. The improvement seen in CNNs over random forest classifiers demonstrates that the spatial data hid in the images contains essential information about the tissue type. CNNs take advantage of this information by extracting spectral-spatial features characteristic of tissue types in the Area surrounding a pixel, thus achieving improved accuracy. Additionally, as the accuracy of random forest classifiers trained on O-PTIR data is much lower than CNN, the greater resolution in O-PTIR imaging likely causes an increase in within-class spectral diversity, meaning the classes are broader and more difficult for a non-spatial model to distinguish. This effect is overcome by the convolutional models, which use spatial features in classification. The comparison of networks trained on O-PTIR data demonstrated a statistically significant improvement in classification accuracy. Therefore, this work shows that the higher resolution of O-PTIR imaging provides additional spectral information, which aids in tissue classification. This result is promising for using IR spectroscopic imaging techniques with improved resolution in refining the accuracy of tissue classification algorithms.

There are multiple ways of improving classification accuracy, and the quality of Annotations has a significant effect on training and testing the accuracy of networks. By improving the accuracy of our epithelial and stromal tissue annotations, network performance would likely improve. Additionally, as annotations are drawn on adjacent tissue sections and manually aligned, there is an inherent error in the ground truth classes, decreasing classifier performance. We also selected five wavenumbers from the mid-infrared spectrum to image with the O-PTIR system and similarly limited the FTIR data to the same wavenumbers as O-PTIR data collection is time-intensive, and the time required to image is directly proportional to the number of wavenumbers. Additional spectral information to distinguish tissue classes could be achieved by adding additional IR wavenumbers to the data. Our

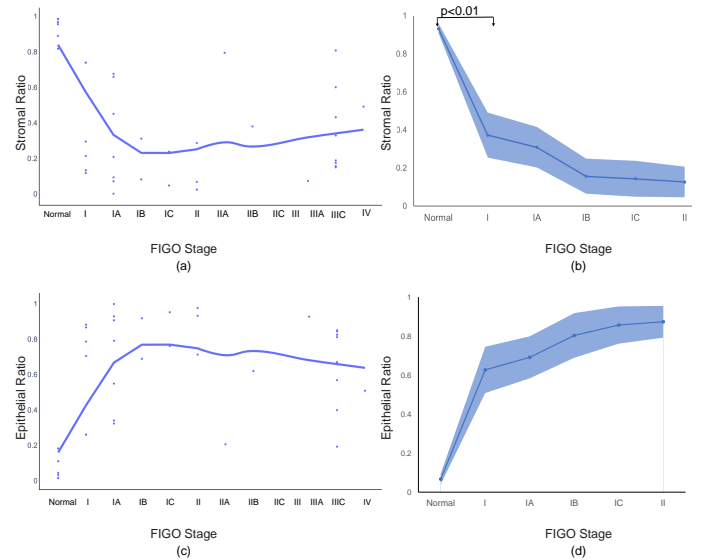


**Fig. 9** Stromal and Epithelial Ratios are plotted as a function of pathological FIGO stage of ovarian cancer. Stromal ratios in panels a-b are calculated by dividing the number of pixels classified as stroma by the total number of pixels, while epithelial ratios in panels c-d are calculated by dividing the number of pixels classified as epithelial by the number of total pixels. The (a) and (c) graph shows a non-linear fit for stromal ratio and epithelial ratio to cancer stage. There is a substantial decrease in stromal ratio and a dramatic increase in epithelial ratio during the early stage of cancer from normal tissue until stage II, which is plotted with the mean and error bands in (b) and (d). P values calculated in figure (b) show that stromal and epithelial amounts significantly differ in normal ovary versus early stages of cancer. Since this is a binary classification, p values remain the same for the plots in panel b and d.

method for wavenumber selection was based on tissue qualities and spectral appearance. More rigorous methods for selection which analyze the deterministic power of a wavenumber could contribute to classification improvement. Further research is necessary for optimal wavenumber selection for O-PTIR imaging.

The effect of improved spatial resolution may be more profound when considering other tissue types in classification, such as blood, adipocytes, or myofibroblasts. Designing classifiers with these tissue types could provide more insight into the magnitude of improvement afforded by additional resolution. Further investigation is necessary in these areas to more fully explore the benefits of O-PTIR spectroscopic imaging.

Stroma to Epithelium ratio is used as one of the important clinical markers to determine the stage of cancer, and from Figure 9 we can demonstrate that there is a significant decrease in the stroma percentage as there is the progression in stages of cancer relative to normal healthy tissue. The Stroma ratio is evaluated per core for each stage of cancer after the CNN model has done complete classification on the entire core. Since CNN output is seen as probabilities, we set a threshold of 80 percent to determine whether a given pixel belongs to epithelium or stroma and calculated the ratio of stroma to the epithelium and stroma pixels while marking the pixels with probabilities less than 80 percent as other class which could correspond to the presence of necrotic tissue, lymphocytes and blood vessels in the tissue.

## 5 Conclusion

The introduction of the O-PTIR spectroscopic imaging technique has significantly improved spatial resolution over the FTIR imaging technique. It is thus essential to consider whether this improvement is consequential in the application. This study is the first analysis of the effect of resolution improvement in IR spectroscopic image data in classification of human tissue to the best of our knowledge. O-PTIR imaging with CNN classification can provide a meaningful improvement in computational and quantitative histopathology, and preliminary results in ovarian tissue histopathology using infrared spectroscopy are promising. This project demonstrates the utility of O-PTIR in ovarian tissue analysis and opens the door for further ovarian cancer studies using O-PTIR.

## Author Contributions

We strongly encourage authors to include author contributions and recommend using CRediT for standardised contribution descriptions. Please refer to our general author guidelines for more information about authorship.

## Conflicts of interest

There are no conflicts to declare.

## Acknowledgements

This work is supported in part by the NLM Training Program in Biomedical Informatics and Data Science T15LM007093 (RM, RR), the Cancer Prevention and Research Institute of Texas (CPRIT) #RR170075 (RR), National Institutes of Health #R01HL146745 (DM), the National Science Foundation CAREER Award #1943455, NLM Training Program in Biomedical Informatics and Data Science #T15LM007093 SB), the NLM 2019 Data Science and Biomedical Informatics Undergraduate Summer Research Program (MB) grant 3T15LM007093-27S1, National Institutes of Health P50 CA217685 (AKS), P30CA016672 (AKS), American Cancer Society Research Professor Award (AKS), Frank McGraw Memorial Chair in Cancer Research (AKS), Moon Shot in Ovarian Cancer (AKS).

## Notes and references

- 1 L. A. Torre, B. Trabert, C. E. DeSantis, K. D. Miller, G. Samimi, C. D. Runowicz, M. M. Gaudet, A. Jemal and R. L. Siegel, *CA: a cancer journal for clinicians*, 2018, **68**, 284.
- 2 S. Lheureux, C. Gourley, I. Vergote and A. Oza, *Lancet (London, England)*, 2019, **393**, 1240.
- 3 J.-M. Lee, L. Minasian and E. C. Kohn, *Cancer*, 2019, **125**, 4623.
- 4 A. du Bois, A. Reuss, E. Pujade-Lauraine, P. Harter, I. Ray-Coquard and J. Pfisterer, *Cancer*, 2009, **115**, 1234–1244.
- 5 S. Kehoe, J. Hook, M. Nankivell, G. C. Jayson, H. Kitchener, T. Lopes, D. Luesley, T. Perren, S. Bannoo, M. Mascarenhas et al., *Lancet (London, England)*, 2015, **386**, 249–257.
- 6 I. Vergote, C. G. Tropé, F. Amant, G. B. Kristensen, T. Ehlen, N. Johnson, R. H. Verheijen, M. E. van der Burg, A. J. Lacave, P. B. Panici et al., *The New England journal of medicine*, 2010, **363**, 943–953.
- 7 Z. Luo, Q. Wang, W. Lau, B. Lau, L. Xu, L. Zhao, H. Yang, M. Feng, Y. Xuan, Y. Yang et al., *Cancer letters*, 2016, **377**, 174.
- 8 E. Banks, *Methods in Molecular Medicine*, 2001, **39**, 3–11.
- 9 A. P. Heintz, F. Odicino, P. Maisonneuve, U. Beller, J. L. Benedet, W. T. Creasman, H. Y. Ngan, M. Sideri and S. Pecorelli, *Journal of Epidemiology and Biostatistics*, 2001, **6**, 107–138.
- 10 A. Malpica, *International journal of gynecological pathology: official journal of the International Society of Gynecological Pathologists*, 2008, **27**, 175–181.
- 11 E. Hernandez, B. Bhagavan, T. Parmley and N. Rosenshein, *Gynecologic oncology*, 1984, **17**, 117–123.
- 12 A. Malpica, M. T. Deavers, K. Lu, D. C. Bodurka, E. N. Atkinson, D. M. Gershenson and E. G. Silva, *The American journal of surgical pathology*, 2004, **28**, 496–504.
- 13 R. Taylor, J. Zeller, R. Lieberman and D. O'Connor, *Gynecologic oncology*, 1999, **74**, 3–6.
- 14 F. Zeppernick and I. Meinhold-Heerlein, *Archives of gynecology and obstetrics*, 2014, **290**, 839–842.
- 15 A. Malpica, M. T. Deavers, C. Tornos, R. J. Kurman, R. Soslow, J. D. Seidman, M. F. Munsell, E. Gaertner, D. Frishberg and E. G. Silva, *The American journal of surgical pathology*, 2007, **31**, 1168–1174.
- 16 K. Bera, K. A. Schalper, D. L. Rimm, V. Velcheti and A. Madabhushi, *Nature reviews. Clinical oncology*, 2019, **16**, 703–715.
- 17 M. Wu, C. Yan, H. Liu and Q. Liu, *Bioscience Reports*, 2018, **38**.
- 18 D. Komura and S. Ishikawa, *Computational and Structural Biotechnology Journal*, 2018, **16**, 34.
- 19 Y. Du, R. Zhang, A. Zargari, T. C. Thai, C. C. Gunderson, K. M. Moxley, H. Liu, B. Zheng and Y. Qiu, *Annals of biomedical engineering*, 2018, **46**, 1988–1999.
- 20 X. Chen, R. Zhang, K.-M. Fung, H. Liu, B. Zheng and Y. Qiu, *Biophotonics and Immune Responses XV*, 2020, p. 112410F.
- 21 J. Xu, C. Zhou, B. Lang and Q. Liu, *Deep Learning and Convolutional Neural Networks for Medical Image Computing*, Springer, 2017, pp. 73–95.
- 22 C. Fiore, D. Bailey, N. Conlon, X. Wu, N. Martin, M. Fiorentino, S. Finn, K. Fall, S.-O. Andersson, O. Andren et al., *Journal of clinical pathology*, 2012, **65**, 496–502.
- 23 I. ur Rehman, Z. Movasaghi and S. Rehman, *Vibrational spectroscopy for tissue analysis*, CRC press, 2012.
- 24 M. J. D'Souza and F. Koyoshi, *Pharmaceutical reviews*, 2009, **7**, <http://www>.
- 25 C. L. Morais, P. L. Martin-Hirsch and F. L. Martin, *Analyst*, 2019, **144**, 2312–2319.
- 26 M. Paraskevaidi, K. M. Ashton, H. F. Stringfellow, N. J. Wood, P. J. Keating, A. W. Rowbottom, P. L. Martin-Hirsch and F. L. Martin, *Talanta*, 2018, **189**, 281–288.
- 27 K. Maheedhar, R. A. Bhat, R. Malini, N. Prathima, P. Keerthi, P. Kushtagi and C. M. Krishna, *Photomedicine and Laser Surgery*, 2008, **26**, 83–90.

28 C. M. Krishna, G. Sockalingum, R. A. Bhat, L. Venteo, P. Kushtagi, M. Pluot and M. Manfait, *Analytical and bioanalytical chemistry*, 2007, **387**, 1649–1656.

29 K. R. Flower, I. Khalifa, P. Bassan, D. Démoulin, E. Jackson, N. P. Lockyer, A. T. McGown, P. Miles, L. Vaccari and P. Gardner, *Analyst*, 2011, **136**, 498–507.

30 K. Gajjar, J. Trevisan, G. Owens, P. J. Keating, N. J. Wood, H. F. Stringfellow, P. L. Martin-Hirsch and F. L. Martin, *Analyst*, 2013, **138**, 3917–3926.

31 G. Theophilou, K. M. Lima, P. L. Martin-Hirsch, H. F. Stringfellow and F. L. Martin, *Analyst*, 2016, **141**, 585–594.

32 K. M. Lima, K. B. Gajjar, P. L. Martin-Hirsch and F. L. Martin, *Biotechnology progress*, 2015, **31**, 832–839.

33 O. Klein, F. Kanter, H. Kulbe, P. Jank, C. Denkert, G. Nebrich, W. D. Schmitt, Z. Wu, C. A. Kunze, J. Sehouli *et al.*, *PROTEOMICS–Clinical Applications*, 2019, **13**, 1700181.

34 A. A. Zeitoune, J. S. Luna, K. Sanchez Salas, L. Erbes, C. L. Cesar, L. A. Andrade, H. F. Carvahlo, F. Bottcher-Luiz, V. H. Casco and J. Adur, *Cancer informatics*, 2017, **16**, 1176935117690162.

35 D. Pouli, E. M. Genega, T. B. Sullivan, K. M. Rieger-Christ, V. Wright, I. Georgakoudi and T. Schnelldorfer, *Biomedical Optics Express*, 2019, **10**, 4479.

36 K. Tilbury and P. J. Campagnola, *Perspectives in medicinal chemistry*, 2015, **7**, PMC–S13214.

37 M. J. Huttunen, A. Hassan, C. W. McCloskey, S. Fasih, J. Upham, B. C. Vanderhyden, R. W. Boyd and S. Murugkar, *Journal of biomedical optics*, 2018, **23**, 066002.

38 J. V. Jokerst, A. J. Cole, D. Van de Sompel and S. S. Gambhir, *ACS nano*, 2012, **6**, 10366–10377.

39 A. Oseledchyk, C. Andreou, M. A. Wall and M. F. Kircher, *ACS nano*, 2017, **11**, 1488–1497.

40 C. Petibois and G. Déléris, *TRENDS in Biotechnology*, 2006, **24**, 455–462.

41 A. Benard, C. Desmedt, M. Smolina, P. Szternfeld, M. Verdonck, G. Rouas, N. Khedoumi, F. Rothé, D. Larsimont, C. Sotiriou *et al.*, *Analyst*, 2014, **139**, 1044–1056.

42 F. Großrueschkamp, A. Kallenbach-Thielges, T. Behrens, T. Brüning, M. Altmayer, G. Stamatis, D. Theegarten and K. Gerwert, *Analyst*, 2015, **140**, 2114–2120.

43 M. J. Baker, E. Gazi, M. D. Brown, J. H. Shanks, N. W. Clarke and P. Gardner, *Journal of biophotonics*, 2009, **2**, 104–113.

44 C. Krafft, D. Codrich, G. Pelizzo and V. Sergo, *Journal of biophotonics*, 2008, **1**, 154–169.

45 M. J. Baker, J. Trevisan, P. Bassan, R. Bhargava, H. J. Butler, K. M. Dorling, P. R. Fielden, S. W. Fogarty, N. J. Fullwood, K. A. Heys *et al.*, *Nature protocols*, 2014, **9**, 1771.

46 F. N. Pounder, R. K. Reddy and R. Bhargava, *Faraday Discussions*, 2016, **187**, 43–68.

47 S. Pahlow, K. Weber, J. Popp, B. R. Wood, K. Kochan, A. Rüther, D. Perez-Guaita, P. Heraud, N. Stone, A. Dudgeon, B. Gardner, R. Reddy, D. Mayerich and R. Bhargava, *Applied spectroscopy*, 2018, **72**, 52–84.

48 D. Zhang, C. Li, C. Zhang, M. N. Slipchenko, G. Eakins and J.-X. Cheng, *Science advances*, 2016, **2**, e1600521.

49 Z. Qin, S. Dai, C. C. Gajjela, C. Wang, V. G. Hadjiev, G. Yang, J. Li, X. Zhong, Z. Tang, Y. Yao *et al.*, *Chemistry of Materials*, 2020.

50 Y. Bai, D. Zhang, L. Lan, Y. Huang, K. Maize, A. Shakouri and J.-X. Cheng, *Science advances*, 2019, **5**, eaav7127.

51 W. Hu, Y. Huang, L. Wei, F. Zhang and H. Li, *Journal of Sensors*, 2015, **2015**.

52 S. Berisha, M. Lotfollahi, J. Jahanipour, I. Gurcan, M. Walsh, R. Bhargava, H. Van Nguyen and D. Mayerich, *Analyst*, 2019, **144**, 1642–1653.

53 V. Zohdi, D. R. Whelan, B. R. Wood, J. T. Pearson, K. R. Bamberg and M. J. Black, *PLoS One*, 2015, **10**, e0116491.

54 D. P. Kingma and J. A. Ba, *arXiv preprint arXiv:1412.6980*, 2019, **434**.

55 S. Berisha, S. Chang, S. Saki, D. Daeinejad, Z. He, R. Mankar and D. Mayerich, *Analyst*, 2017, **142**, 1350–1357.

56 F. Chollet *et al.*, *Keras*, <https://keras.io>, 2015.

57 M. Abadi, A. Agarwal, P. Barham, E. Brevdo, Z. Chen, C. Citro, G. S. Corrado, A. Davis, J. Dean, M. Devin, S. Ghemawat, I. Goodfellow, A. Harp, G. Irving, M. Isard, Y. Jia, R. Jozefowicz, L. Kaiser, M. Kudlur, J. Levenberg, D. Mané, R. Monga, S. Moore, D. Murray, C. Olah, M. Schuster, J. Shlens, B. Steiner, I. Sutskever, K. Talwar, P. Tucker, V. Vanhoucke, V. Vasudevan, F. Viégas, O. Vinyals, P. Warden, M. Wattenberg, M. Wicke, Y. Yu and X. Zheng, *TensorFlow: Large-Scale Machine Learning on Heterogeneous Systems*, 2015, <http://tensorflow.org/>, Software available from tensorflow.org.

58 F. Pedregosa, G. Varoquaux, A. Gramfort, V. Michel, B. Thirion, O. Grisel, M. Blondel, P. Prettenhofer, R. Weiss, V. Dubourg, J. Vanderplas, A. Passos, D. Cournapeau, M. Brucher, M. Perrot and E. Duchesnay, *Journal of Machine Learning Research*, 2011, **12**, 2825–2830.